ARTICLE

Structure and electrochemical properties of hierarchically porous carbon nanomaterials derived from hybrid ZIF-8/ZIF-67 bi-MOF coated cyclomatrix poly (organophosphazene) nanospheres

Received 00th January 20xx,
Accepted 00th January 20xx

DOI: 10.1039/x0xx00000x

Yutao Zhou[a], Alan M. Wemyss[a], Oliver B. Brown[a], Qianye Huang[b], Chaoying Wan[a]*

Hybrid bi-ZIF nanocrystals consisting of ZIF-8/ZIF-67 were synthesised in the presence of cyclomatrix poly(organophosphazene) (POP) nanospheres and formed POP/bi-ZIF core@shell nanospheres. The POP/bi-ZIF showed excellent thermal stability up to 478°C, with well-preserved core@shell structures during carbonization at 850°C. The resultant core@shell carbon nanospheres exhibited hierarchically mesoporous structures. The porous carbon core was derived from the carbonised covalent inorganic-organic polyphosphazene framework, containing *in situ* doped heteroatoms such as N, P, S and O; the shell structure was derived from the bi-ZIF containing up to 40% of Zn and Co elements. The bi-ZIF derived carbon shell showed a BET surface area of 1347.76 $m^2 g^{-1}$ and a Langmuir surface area of 1882.71 $m^2 g^{-1}$, and the total BET surface area of the core@shell structure reached 1025.00 $m^2 g^{-1}$. When applied as an anode material in lithium ion batteries, the core@shell carbon structure reached a charge capacity of 595 mA h g^{-1} with a discharge capacity of 546 mA h g^{-1}, and remained reversible charge/discharge capacity at 400 mA h g^{-1} after 140 cycles, which is higher than the theoretical capacity of graphite anode. A good cycling stability with 83% capacity retention in the C-rate tests was achieved. This work provides a facile and scalable method to produce mesoporous carbon nanostructures with *in situ* doped metal elements and heteroatoms, which benefits the high rate electrochemical properties of lithium ion batteries.

1. Introduction

Lithium-ion batteries (LIB) have played an important role in modern technologies, from portable electronic devices, hybrid electric vehicles to grid scale energy storage systems.[1-3] The ultimate goal of high performance LIBs is to achieve a combination of high energy and power densities, low environmental impact, long cycle life and safe operation.[4, 5] Extensive research activities has been invested in developing active materials for battery components, including cathodes, anodes, electrolytes, functional binders and separators. New and functional electrode materials can potentially increase the practical specific energy limit of current LIB, Li-S and Li-O systems, for example the $Li_{4.2}Si$ electrode can reach a capacity of 897 mA h g^{-1}, nearly double of the traditional LiC_6/layered $Li_{1-x}MO_2$ batteries of 584 mA h g^{-1}.[6]

Zeolitic imidazolate frameworks (ZIFs), a subcategory of metal organic frameworks (MOFs), show a combination of high thermal and chemical stability, coupled with high chemical tunability.[7-9] ZIF materials consist of divalent tetrahedral metal cations, typically but not exclusively Zn^{2+} or Co^{2+}, connected by imidazole (1-MI or Hmim) units, which grow into complex rhombic dodecahedral structures.[7, 10, 11] ZIF-67 is a Co-based framework material and typically collapses at temperatures of 600°C and above. In comparison, Zn-based ZIF-8 crystals are more thermally stable, and undergo 'evaporation' during carbonisation leading to mesoporous carbon nanoparticles with high surface area.[12-15] However, ZIF-8 suffers from poor electrical conductivity, the Zn^{2+} is reported to be 1000 times less conductive than Co^{2+}.[8] Core@shell structures of ZIF-67@ZIF-8 with ZIF-67 as the core and coated with a ZIF-8 shell was reported.[16] A subsequent carbonisation of the ZIF-67@ZIF-8 core@shell structures resulted in hierarchically mesoporous carbon structures with *in situ* doped heteroatoms, showing high porosity, large surface areas, and low densities, which are potential active materials for LIBs applications.[17-19] However, the low electrical conductivity of ZIF-8, and structural instability of ZIF-67, in particular under the carbonisation conditions,[12, 13] have highly limited their applications in batteries.

A hybrid combination of ZIF-8 and ZIF-67 crystals can synergise the structural stability of the two crystal structures.[16] The hybrid ZIF structures were synthesised by mixing zinc nitrate hexahydrate and cobalt nitrate hexahydrate with 2-methylimidazole following a general synthetic route for ZIFs. Compared with the ZIF-8 synthesis procedure, the metal Co can substitute Zn without changing the topology.[20] The Co was reported to form cobalt oxide during carbonisation, which increases the electrical conductivity of the bi-ZIF derived porous carbon materials.[8, 12]

Bi-ZIFs typically retain the crystal structure and topology of their individual ZIF networks, which has been observed through

[a] *International Institute for Nanocomposites Manufacturing (IINM), WMG, University of Warwick, CV4 7AL, UK. Email: Chaoying.wan@warwick.ac.uk*
[b] *Energy Innovation Centre (EIC), WMG, University of Warwick, UK, CV4 7AL*
Electronic Supplementary Information (ESI) available: [details of any supplementary information available should be included here]. See DOI: 10.1039/x0xx00000x

multiple XRD studies.[13, 21, 22] The sizes of bi-ZIF crystals depend on the composition ratios, there is no observable effect on the bi-ZIF crystal size when the Co^{2+} content is 2-10 mol% of all metal content.[22] At Zn : Co ratios of 8:2, 6:4, 4:6 and 2:8, the crystal sizes were varied from 15-30 nm, 30-40 nm, 60-70 nm to 85-170 nm, respectively.[23] The content of Zn^{2+} is found to affect the porosity and BET surface area of the bi-ZIF. For instance, the surface area of bi-ZIF increased from 323 $m^2 g^{-1}$ to 853 $m^2 g^{-1}$, and total pore volume increased from 0.68 $cm^3 g^{-1}$ to 1.24 $cm^3 g^{-1}$, were observed when the Zn : Co ratio was increased from 6:2 to 7.5:0.5.[14] Another study reported that at Zn : Co ratios of 8:2, 6:4, 4:6 or 2:8, the BET surface area of the resulting bi-ZIFs was 1331 m^2g^{-1}, 1513 m^2g^{-1}, 1319 m^2g^{-1} or 1308 $m^2 g^{-1}$, respectively.[23] Interestingly this suggests a peak ratio for a maximum BET surface area as a function of the Zn : Co ratio, as oppose to a linear increase with Zn composition, as reported by other studies.[24]

One study investigated a ZIF-67@bi-ZIF using a range of Zn : Co ratios that showed good tunability in particle size and morphology, with the possibility of forming core@shell structures.[25] Another investigated growing Zn/Co-ZIF onto ZnO nanowires decorated by Co/CoS_2 nanoparticles with Fe atoms showing a high Li-ion battery capacity of 1325 mA h g^{-1}.[25, 26] Polyaniline@bi-ZIF core@shell structures were reported using a variety of Zn : Co molar ratios, when used as ORR catalyst, they reached an onset potential of -0.099 V and half-wave potential of -0.20 V vs. Ag/AgCl.[27]

Core@shell carbon nanostructures are often used for energy storage applications, as the structures are facilely tailored by the synthetic conditions and compositions. In some cases, the core or shell structure is used as a sacrificing template,[28] in particular if one of the components is expensive, then the cheaper template filling material lowers the cost without compromising the functions.[29] How to balance a core@shell structure to utilise and synergise the properties of the core and shell materials is key to exploiting the full potential of the materials.

In this work, we introduced cyclomatrix poly(organophosphazene) (POP) nanospheres as the core material, bi-ZIF as the shell. POPs are covalently crosslinked frameworks with high contents of heteroatoms, such as N, S, P, Cl and O. The synthesis of POP nanospheres is achieved under one-pot ambient conditions, and can be further transformed into porous carbon spheres with well-preserved morphology and *in situ* doped heteroatoms.[30] The coating of bi-ZIF onto POP spheres is expected to generate a synergistic effect, where both heteroatoms and transition metals provide redox active sites on the resulting carbon nanomaterials.[31] The presence of cobalt and nitrogen can also improve the surface area and wettability of the carbon electrode,[32] benefiting the transportation of electrons and protons.[33]

Here, mono-dispersed bi-ZIF crystals were synthesised with optimised reaction conditions. The effects of the Zn:Co:Hmim:MeOH ratios and growth time on the particle size and distribution were investigated. POP nanospheres were synthesised under sonication at ambient conditions, which was applied as a core material to allow a subsequent coating of the bi-ZIF crystals to form POP/bi-ZIF core@shell spheres. A following carbonisation process turned the core@shell structures into mesoporous carbon nanopheres. The structure and electrochemical properties of the core@shell structured nanocarbon were evaluated for anode materials for LIBs.

2. Experimental

2.1 Materials

Zinc nitrate hexahydrate (98%), cobalt nitrate hexahydrate (98%), 2-methylimidazole (97%), sodium formate (ACS Grade), 1-methylimidazole (99%) were purchased from VWR International Ltd. (UK). Hexachlorocyclotriphosphazene (HCCP), 4,4-sulphonyldiphenol (BPS) were purchased from Sigma-Aldrich, UK, and triethylamine (TEA) and CH_3CN were purchased from Fisher Sci, UK. All chemicals were used as received without further purification.

2.2 Synthesis of ZIF-8/ZIF-67 bi-ZIF particles

For the synthesis of bi-ZIF particles with a Co:Zn ratio of 7:3, 1.450 g $Co(NO_3)_2{\cdot}6H_2O$ and 0.600 g $Zn(NO_3)_2{\cdot}6H_2O$ were dissolved into 45 mL MeOH and the solution was stirred gently for 10 mins. Separately, 2.690 g Hmim was dissolved in 45 mL MeOH and this solution was added dropwise to the Co/Zn solution, which was then stirred for 24 hrs. The dispersion was then centrifuged and washed in MeOH before being vacuum-dried overnight at 60°C. Conditions for the formation of the other pure bi-ZIF samples are given in Table 1.

2.3 Synthesis of POP/bi-ZIF core@shell nanomaterials

A schematic illustration of the synthesis is given in Figure 1. In a typical reaction, 0.061 g HCCP and 0.138 g BPS were dissolved in 100 mL acetonitrile and sonicated for 5 mins. 3 mL of TEA was then added and the mixture was stirred for 2 hrs. The dispersion was then centrifuged and the pellet was washed with MeOH before being redispersed in 32 mL MeOH through sonication for 3 hrs. Different amounts of $Co(NO_3)_2{\cdot}6H_2O$ and $Zn(NO_3)_2{\cdot}6H_2O$ were added to the POP solution followed by stirring for 5 mins. 1.6 g Hmim were then dissolved in 32 mL MeOH before being added dropwise to the POP/Zn/Co solution. The solution was stirred for 3 hrs then centrifuged and washed with MeOH before being vacuum-dried over night at 60°C. Conditions for other POP/Bi-ZIF synthesis are shown in Table 2.

Table 1 Reaction conditions for ZIF-8/ZIF-67 bi-ZIF particles

bi-ZIF Sample	Co:Zn:Hmim:MeOH (Molar ratio)	Growth Time (hrs)
A	0.1:0.9:6:500	A1, A3, A6 (growth time 1, 3, 6 hrs)
B	0.5:0.5:6:500	A1, A3, A6 (growth time 1, 3, 6 hrs)
C	0.9:0.1:6:500	C1, C3, C6 (growth time 1, 3, 6 hrs)
D	0.1:0.9:4:675	D1, D3, D6 (growth time 1, 3, 6 hrs)

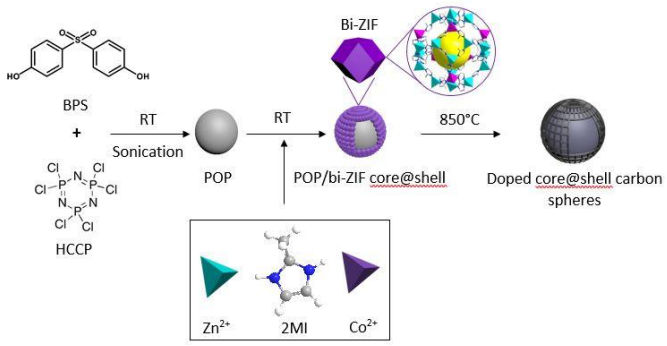

Figure 1 Schematic illustration of the synthesis and carbonization of POP/bi-ZIF core@shell structures

2.4 Carbonisation of core@shell structures

Carbonisation of bi-ZIF and POP/bi-ZIF samples were conducted at the same condition in a tube furnace. The samples were heated from 25°C to 850°C at a heating rate of 5°C/min, and held at 850°C for 2 hrs, then naturally cooled down to 25°C. The carbonisation processes were conducted under a nitrogen atmosphere.

2.5 Characterisation

Field emission gun-scanning electron microscopy (FEG-SEM) and X-ray electron dispersive spectroscopy analysis (EDX) were accomplished using a Zeiss SIGMA SEM. Gold-palladium sputtering was applied to the uncarbonised samples before analysis. The carbonised samples can be observed without coating due to their good electrical conductivity. Raman spectra were obtained with a Renishaw spectrometer equipped with 532 nm laser. Thermogravimetric analyses (TGA) were conducted with a Mettler Toledo instrument in the temperature range of 25~850°C at a heating rate of 10°C min−1 under N2 gas flow (30 mL min−1). Specific surface areas were calculated from the nitrogen adsorption-desorption isotherm curves recorded by a Micromeritics ASAP 2020 Physisorption Analyzer (0.0-1.0 P/Po). The samples were degassed at 120°C for 3 hrs under high vacuum before measurements. The powder X-ray diffraction (XRD) patterns were obtained by using a Panalytical Empyrean diffractometer with a CoKα radiation source (1.7929 Å) operated at 40 kV and 40 mA. The scanning step was 0.013° 2θ. For electrochemistry analysis, a slurry paste containing carbonised POP/bi-ZIF (850°C, 73 wt%), carbon black (18 wt%) and PVDF binder (9 wt%) was prepared in N-methyl-2-pyrrolidone. The slurry was casted on a copper foil (as energy storage electrode) with a blade gap of 80 µm, and then dried overnight in a vacuum oven before assembling into a coin cell (type 2032 format). Half-cells were constructed using an lithium foil as reference and a counter electrode. Celgard 2325 microporous membrane was used as the separator material. 1M LiPF6 in ethylene carbonate: ethylmethyl carbonate (3:7 volume ratio) and 1 wt% vinylene carbonate was used as the electrolyte. Electrochemical impedance spectroscopy (EIS) was used to measure the impedance change along with cycle times. The test was conducted with voltage amplitude of 10 mV, measured between frequencies of 400 kHz and 100 mHz at fully lithiation status of each cell. The first measurement was taken after the formation cycle with additional 10 min of relaxation time, and then repeated every 20 cycles.

3. Results and Discussion

3.1 Effect of synthesis conditions on the structures of bi-ZIFs

The effect of synthesis conditions on the structures of bi-ZIF particles was investigated by varying the Co:Zn ratio, growth time, and the system concentration (Metal : Hmim : MeOH ratio). The morphology of bi-ZIF crystals, with Co:Zn ratios of 1:9, 5:5 and 9:1 are given in Figures 2A, 2B and 2C, respectively. Figure 2D shows the particle size and distribution of the samples. These results show that the particle size increases from 164 ± 60 nm for Co:Zn = 1:9, to 297 ± 120 nm for Co:Zn = 5:5, and then to 337 ± 130 nm for Co:Zn = 9:1. The size dispersity increases with Co content. These results are in line with previously reported studies, which showed that the increase of Co content of precursor materials resulted in larger bi-ZIF crystals.[13, 21, 23]

Table 2 Reaction conditions for POP/bi-ZIF Core@Shell structures

POP/bi-ZIF	HCCP (g)	BPS (g)	Co^{2+} (g)	Zn^{2+} (g)	Hmim (g)	MeOH (mL)	Co:Zn: Hmim:MeOH (Molar ratio)	Growth Time (hr)
POP/bi-ZIF (Sample A1)	0.061	0.138	0.093	0.860	1.6	32×2	0.1:0.9: 6:500	1
POP/bi-ZIF (B1)	0.061	0.138	0.466	0.476	1.6	32×2	0.5:0.5: 6:500	1
POP/bi-ZIF (C1)	0.061	0.138	0.841	0.095	1.6	32×2	0.9:0.1: 6:500	1
POP/bi-ZIF (D1)	0.061	0.138	0.698	0.239	1.6	32×2	0.75:0.25: 6: 500	1
POP/bi-ZIF (E1)	0.061	0.138	0.233	0.717	1.6	32×2	0.25:0.75: 6:500	1

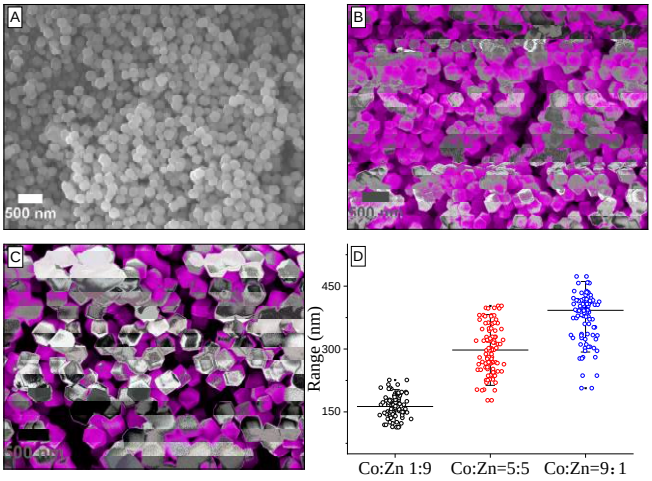

Figure 2 Effect of Co:Zn ratio on the morphology development of bi-ZIF within 3hrs: A) Sample A3 (Co:Zn = 1:9) B) Sample B3 (Co:Zn = 5:5) C) Sample C3 (Co:Zn = 9:1) and D) Particle size and distribution

Figure 3 compares the morphology of bi-ZIF crystals that were prepared with the same Co:Zn ratio (1:9) and system concentration, but different synthesis time. It is shown that longer growth time led to a larger bi-ZIF particle size and slightly wider distribution. The diameter of the particles changed from 125 ± 25 nm after 1 h, 164 ± 60 nm for 3 h and 179 ± 70 nm for 6 h, which corresponds to relative standard deviations (RSD) of 20.00%, 36.59%, and 39.11%, respectively.

The effect of reactant concentration is shown in Figure 4. With a $Metal_{Zn+Co}$: Hmim : MeOH ratio of 1:6:500, the size distribution achieved was 179 ± 70 nm (RSD = 39.11%). The system of $Metal_{Zn+Co}$: Hmim : MeOH ratio of 1:4:675 produced particles with a size of 61 ± 40 nm, an RSD of 65.57%. When the Hmim concentration is low, as in the case of 1:4:675, the shortage of a bridging ligand reduced both the rates of nucleation and crystal growth, resulting in smaller particle sizes and broad size distributions.[34]

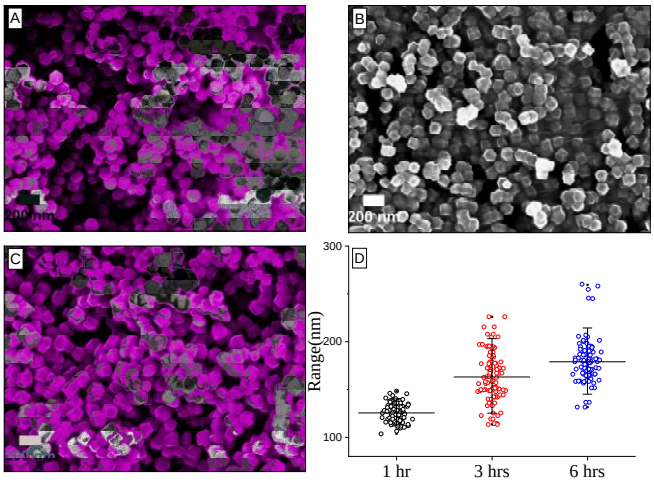

Figure 3 Effect of growth time on the morphology development of bi-ZIF (Co:Zn=1:9) crystals: A-C) Sample A1, A3, A6 and D their particle size distributions

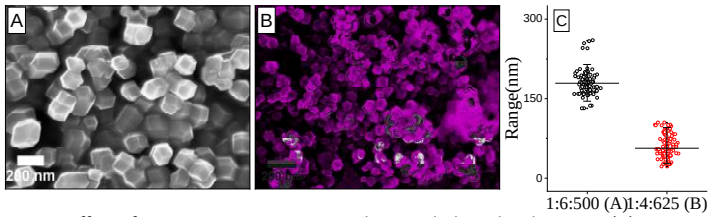

Figure 4 Effect of reactant concentration on the morphology development: (A) A6, $Metal_{Zn+Co}$: Hmim : MeOH = 1:6:500; (B) D6, $Metal_{Zn+Co}$: Hmim : MeOH = 1:4:625; and (C) their particle size distribution

3.2 POP/bi-ZIF core@shell structures

Samples with a Co : Zn ratio of 1:9 are more homogeneous, with average particle sizes of 125 ± 25 nm as shown in Figure 3. They were further applied to prepare POP/bi-ZIF core@shell structures. In our previous work with ZIF-8, we showed the morphology of ZIFs can be affected by the presence of substrates.[31] Here Co:Zn ratios of 2.5:7.5, 5:5, and 7.5:2.5 were also studied to investigate the effect of Co:Zn ratio on the morphology of POP/bi-ZIF core@shell structures.

The morphology of POP/bi-ZIF samples are compared in Figure 5. When the Co:Zn molar ratio is 9:1, the large particles resulting from the higher Co content could inhibit the deposition of the bi-ZIF onto POP surfaces, as shown in Figure 5A, where the POP nanospheres and bi-ZIF decahedrons are mostly separated. Other samples with Co:Zn molar ratio from 7.5:2.5 to 1:9 succeeded in forming core@shell structures with POP nanospheres. In agreement with the results from the bi-ZIF synthesis above, the POP/bi-ZIF sample with lower Co content is more monodispersed, as shown in Figure 5E. Samples with Co:Zn molar ratios of 7.5:2.5, 5:5 and 2.5:7.5 all showed a certain degree of agglomeration of the core@shell particles. Co^{2+} could increase the growth rate of bi-ZIF particles, which can cause aggregation.[34, 35]

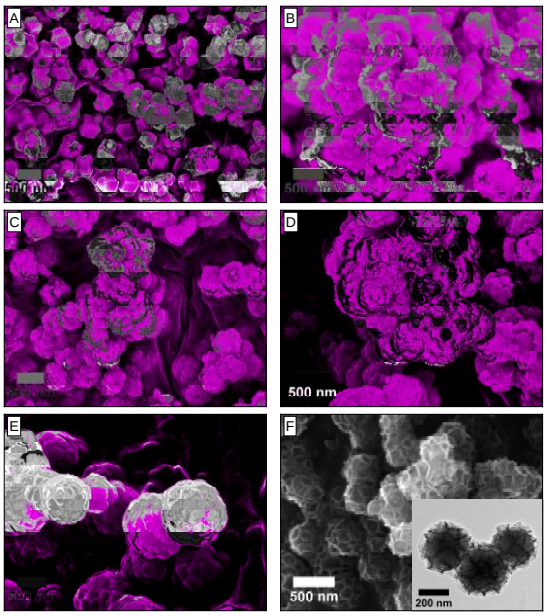

Figure 5 SEM images of (A-E) POP/bi-ZIF samples with different Co:Zn ratios and 1 hr synthesis time. F) carbonized POP/bi-ZIF-A1

The sample in Figures 5E with Co:Zn ratio of 1:9 showed good coverage of the core structure and crystal formation, and more evenly distributed core@shell structures. The surface hydroxyl groups of POP spheres may help the binding and distribution of Zn^{2+} and Co^{2+} cations on the POP surfaces,[30] which further react with the Hmim from the solution and form homogeneous ZIF crystals on the POP surface. Higher Co:Zn ratios resulted in larger bi-ZIF particle sizes. This is because of the slower nucleation process of Co^{2+} salt.[23] Therefore, a higher Zn content results smaller and more homogeneous bi-ZIF particles as compared to those with higher Co content.

3.3 Structure characterisation of POP/bi-ZIF core@shell structures

POP/bi-ZIF core@shell samples synthesised under the condition of A1 and D1 (shown in Table 2) were characterised in detail, as they represented the bi-ZIFs with highest and lowest Co:Zn ratios that successfully formed core@shell structures with POP. The FTIR spectra of the bi-ZIF compounds, synthesised with and without POP nanospheres, are given in Figure 6A and Figure S1, respectively. The spectra of ZIF-8, ZIF-67 and bi-ZIF (A1 and D1) are in good agreement with previously reported FTIR spectra, with characteristic bending and stretching peaks from the Hmim units, observed in the 600-1350 cm^{-1} and 1350-1500 cm^{-1} regions, respectively.[36-38] This implies that the bi-ZIFs (A1 and D1) have similar structures to their individual mono-metal ZIF counterparts. The XRD results of the ZIF-67, bi-ZIF-A1 and POP/bi-ZIF-A1 show almost identical diffraction patterns as shown in Figure 6B, indicating that the bi-ZIF preserves its crystal structure in the POP/bi-ZIF-A1 core@shell material. Both XRD and FTIR results confirmed that irrespective of the Co:Zn ratio and crystal morphology, the formation of POP/bi-ZIF core@shell structures preserves the structural independence of the core and shell components, and shows high structural stability.

TGA was used to investigate the thermal stability of the core@shell particles. As shown in Figure 6C, the sample with highest Co:Zn molar ratio of 9:1, which is the only one that was not able to form a core@shell structure with POP nanospheres, showed the lowest decomposition temperature of 380°C. Other samples with Co:Zn molar ratios from 1:9 to 7.5:2.5 successfully formed core@shell structures and showed higher decomposition temperatures around 478°C. These core@shell materials showed similar thermal stability despite containing different Co:Zn molar ratios. These results suggest that the bi-ZIF and POP remain in their original form in the core@shell structures. For the material with Co:Zn molar ratio of 9:1, the higher Co ratio resulted in a larger size of bi-ZIF particles (Figure 5A), and no POP/bi-ZIF core@shell structures were formed, so the lower decomposition temperature was caused by the decomposition of POP nanospheres, followed by the decomposition of bi-ZIF structures. The TGA results of ZIF-8 and ZIF-67 are given in Figure 6D for comparison. The decomposition time of ZIF-67 and ZIF-8 are 536 °C and 560 °C, respectively. The thermal stability of bi-ZIF in the core@shell structure was slightly lower than original ZIFs due to the fact that the presence of heteroatoms could accelerate the decomposition of the carbon structure. The decomposition temperatures still remained at a high level.

The porosimetry results of both bi-ZIF-A1 particles and POP/Bi-ZIF-A1 core@shell structures are given in Figure 7. The bi-ZIF sample in Figure 7A showed a typical micro-porous absorption curve, with a BET surface area of 1322.52 $m^2 g^{-1}$ and a Langmuir surface area of 1845.67 $m^2 g^{-1}$. The POP/bi-ZIF particles also showed an excellent porosimetry results (Figure 7B), where a BET surface area of 845.77 $m^2 g^{-1}$ and a Langmuir surface area of 1181.71 $m^2 g^{-1}$ were recorded. The results showed that the both bi-ZIF and POP/bi-ZIF core@shell structure inherit the high surface area from mono-metal ZIFs, such as ZIF-8 and ZIF-67.

3.4 Carbonization of POP/bi-ZIF core@shell nanospheres

The POP/bi-ZIF-A1 core@shell structures were further converted into carbon nanostructures by carbonisation at 850°C. The relative concentrations of the main elements in sample A1 and D1 are detected by EDX and shown in Table 3. For the bi-ZIF-A1, Zn and Co contents are 2.4 wt% and 0.3 wt%, and the heteroatom contents were low, except for N which reached 24 wt%. The bi-ZIF-D1 sample shows a similar elements content but with higher Co content of 3.4 wt% and lower Zn content of 0.5 wt%. This is due to the large concentration of carbon inside the composites. After carbonization, the element ratios of bi-ZIF changed dramatically. In carbonized Sample A1, the Zn reached 56.9 wt% with 8.7 wt% Co. N remained at a high level of 24.6 wt%, with P (0.1 wt%), S (0.6 wt%) and O (2.1 wt%). In carbonized Sample D1, the Co reached 51.6 wt% with Zn (7.8 wt%) and N (27.4 wt%). The carbonized POP/bi-ZIF core@shell structure showed well-distributed element contents of both metal and heteroatoms. The cabonized POP/bi-ZIF-A1 had Zn (28.8 wt%) and Co (10.3 wt%), with N (4.8 wt%), P (14.2 wt%), S (4.8 wt%) and O (28.1 wt%). In comparison, the cabonized POP/bi-ZIF-D1 had Zn (1.4 wt%), Co (35.7 wt%), N (7.5 wt%), P (3.8 wt%), S (4.5 wt%) and O (20.5 wt%). The abundance of metals and heteroatoms, such as Zn, Co, N, P and S, will help increase the number of reactive sites for the pseudo/redox reaction on the anode in lithium ion batteries, contributing to capacity directly, as well as increase the wettability of the anode material and benefit the electrochemical performance.

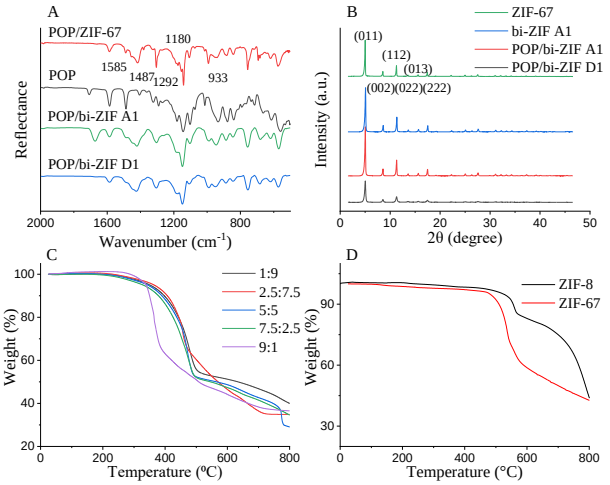

Figure 6 A) FTIR results of POP, POP/ZIF-67, POP/bi-ZIF-A1, POP/bi-ZIF-D1, B) Powder XRD patterns of ZIF-67, bi-ZIF-A1, POP/bi-ZIF-A1 and POP/bi-ZIF-D1; (C) TGA results of POP/bi-ZIF core@shell samples with different Co:Zn molar ratios and (D) TGA results of ZIF-8 and ZIF-67.

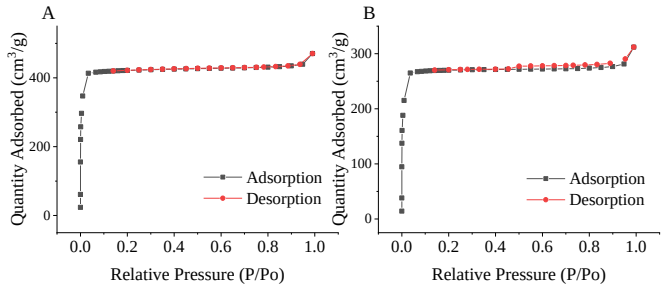

Figure 7 Porosimetry results of A) bi-ZIF and B) POP/bi-ZIF-A1core@shell structure

According to the TGA analysis, the bi-ZIF started to decompose at 573°C, and the bi-ZIF/POP-A1 core@shell structure started to decompose at a slightly lower temperature of 478°C (Figure S2A). The Raman spectrum of a POP/bi-ZIF structure is given in Figure S2B. The G and D peak can be observed at 1350 cm^{-1} and 1590 cm^{-1}, respectively. The D band represents the defected/disordered graphite structure, which was caused by the different dopants of metal and heteroatoms. The G band shows the presence of crystalline graphite carbon. By peak area determination, the ratio of different kinds of carbon can be calculated. From the spectrum in Figure S2B, the carbonized POP/bi-ZIF was made up by 75% of amorphous carbon and 25% of graphitic carbon.[39]

3.5 Electrochemical analysis

The POP/bi-ZIF derived carbon core@shell nanospheres showed high surface area, structural consistency, metal/heteroatoms contents and thermal stability, which is beneficial for anode materials for LIBs. The synergy of the core@shell structure and the heteroatoms is investigated through electrochemical analysis of the POP/bi-ZIF (A1 and D1) samples, where A1 (Co:Zn=1:9) has the highest Zn content while D1 (Co:Zn=7.5:2.5) has the highest Co content. By comparing the two samples, the influence of bi-metal in the core@shell structure and their electrochemical performance can be illustrated.

Coin cells containing carbonized POP/bi-ZIF (A1 and D1) prepared anode materials were tested with a series of charge and discharge cycles. A total of 140 cycles were performed. The operating window of the test was set between 0.01 and 0.2 V *vs* Li/Li^+ with a current density of 74 mA g^{-1}. Based on the EIS spectra of the electrodes, the fitting equivalent circuit is shown in Figure 8. It consists of a resistor, representing series resistance, and is followed by a series of three resistors in parallel with a constant phase element and a Warburg diffusion element at the end. They account for the solid electrolyte interphase (SEI) resistance, charge transfer resistance and diffusion impedance, respectively.

As shown in Figure 9C, the 1st cycle of POP/bi-ZIF-A1 (Co:Zn=1:9) showed a 595 mA h g^{-1} charge capacity with a 546 mA h g^{-1} discharge capacity, which was consistent with the typical findings for lithium-ion insertion and solid electrolyte interface formation on anode material of lithium-ion battery. [40] Even after 140 cycles the capacity is still higher than when a graphite anode material is used, with a reduction of less than 4 mA h g^{-1} capacity from the 40th cycle to the 140th cycle, ending at 400 mA h g^{-1}. The initial capacity loss is mainly due to electrolyte decomposition, which also caused a low initial columbic efficiency.[41-43] The specific capacity (both charge and discharge) results demonstrated a better performance than the theoretical capacity of the traditional graphite anode throughout the cycling, which is 372 mA h g^{-1} in the Li ion battery.[44] The increased capacity could result from the rich heteroatom and transition metal content for the same reasons stated previously: the transition metal with heteroatoms can increase the capacity by providing pseudo/redox reaction sites, they can also improve the wettability of the anode material which reduce the resistance in transporting Li^+ and electrons.[45] The high stability of POP/bi-ZIF material assisted the smooth performance of the anode material throughout the 140 cycles, with a high surface area structure that benefits the transport of the electron/Li^+.

For comparison with sample A1, a coin cell containing carbonized POP/bi-ZIF-D1 (Co:Zn=7.5:2.5) was tested in the same way. As show in Figure 9F, the first cycle of D1 showed a 451 mA h g^{-1} charge capacity with 386 mA h g^{-1} discharge capacity, which are both lower than A1. The capacity then dropped under 372 mA h g^{-1} after 2 cycles for discharge capacity and 1 cycle for charge capacity, meaning that the capacity had already dropped under the graphite's theoretical capacity of 372 mA h g^{-1}. The reasons of the relatively low capacity performance of D1 could be the large particle size. When Co is at the anode of Li ions battery, the content Co is not directly involved in the insertion and extraction of the Li^+, nor the electrochemical reaction at the electrode. The main driving force increasing the capacity that Co is contributing to is the pseudocapacitance.[42] Pseudocapacitance is much related to the size of the material. The path of transporting Li^+ will be longer with larger particle sizes, which will lead to the loss of capacity performance.[46] The findings from the battery tests above are in accordance with this hypothesis of capacity loss caused by large particle sizes, as the POP/bi-ZIF-D1 core@shell material had a much thicker bi-ZIF covers than POP/bi-ZIF-A1 core@shell structure, the large particle size will restrain the pseudocapacitance contributing to the capacity. This is a common problem of battery anode materials containing high content of Co in ZIFs structures.[40]

Table 3 EDX characterization of bi-ZIF-A1 and bi-ZIF-D1 based samples

Key Element (wt%)	bi-ZIF-A1	bi-ZIF-D1	Carbonized bi-ZIF-A1	Carbonized bi-ZIF-D1	Carbonized POP/bi-ZIF-A1	Carbonized POP/bi-ZIF-D1
Zn	2.4	0.5	56.9	7.8	28.8	1.4
Co	0.3	3.4	8.7	51.6	10.3	35.4
N	24	25.7	24.6	27.4	4.8	7.5
P	-	-	0.1	0.1	14.2	3.8
S	-	-	0.6	0.6	4.8	4.5
O	12.5	16.4	2.1	2.9	28.1	20.5

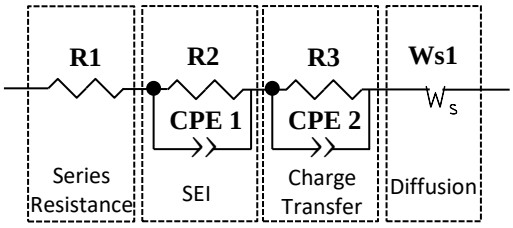

Figure 8 The equivalent circuit used for fitting the impedance spectra

Figure 9A and 9D show charge/discharge capacity (mA h g^{-1}) and columbic efficiency (%) of the constant current cycling profile of both sample A1 and D1. The recorded capacities steadily dropped to a lower value during the earlier part of cycling, which is a typical observation due to solid electrolyte interphase (SEI) formation on anode material of a Li-ion battery. Towards the end of the 140 cycles, the POP/bi-ZIF A1 battery showed a high degree of stability, with a recorded reversible 397/400 mA h g^{-1} charge and discharge capacities (i.e. 100% columbic efficiency). The higher ZIF-8 loading ratio to the core@shell structure can increase the anode capacity and cycling stability over time; hence offering materials with enhanced anode performance for lithiation and de-lithiation processes in LIBs. Towards the end of 140 cycles, POP/bi-ZIF D1 also showed high stability with less than 30 mA h g^{-1} capacity loss from the 40th cycle to the 140th cycle, with a recorded reversible 209/208 mA h g^{-1} charge and discharge capacity.

Figure 9B shows the power extraction capability results of the carbonized POP/bi-ZIF-A1 as an anode material. The discharge capacities were: 541 mA h g^{-1} (0.1 C initially), 422 mA h g^{-1} (0.2 C), 356 mA h g^{-1} (0.5 C), 301 mA h g^{-1} (1 C) and 449 mA h g^{-1} (finishing back to 0.1 C). The capacity retention reached 83% after finishing back to 0.1 C. The results suggests great cycling stability through a scope of power extraction values. Figure 9E shows the power extraction capability results of carbonized POP/bi-ZIF D1. Here, the discharge capacities were: 419 mA h g^{-1} (0.1 C initially), 267 mA h g^{-1} (0.2 C), 240 mA h g^{-1} (0.5 C), 231 mA h g^{-1} (1 C) and 255 mA h g^{-1} (finishing back to 0.1 C). The results are significantly lower than A1, with a capacity retention of just 61% after finishing back to 0.1 C. The poor rate stability results from D1 is caused by its poor overall cycling capacity performance.

Both carbonized ZIF-8 and ZIF-67 showed poor capacity and rate stability, where ZIF-8 showed less than 350 mA g^{-1} after 20 cycles, and ZIF-67 showed less than 200 mA g^{-1} after the 3rd cycle.[31, 40] The pure graphite anode suffered from huge capacity fading after 100 cycles with less than 300 mA g^{-1} of initial capacity in Li/graphite half-cell.[47] The carbonized POP/bi-ZIF core@shell structure showed enhanced performance compared with graphite.

The electrochemical impedance spectroscopy of half cells involving the POP/bi-ZIF-A1 and POP/bi-ZIF-D1 composite electrodes, given in Figure 10, present the impedance developments during cycling. Figure 10 (C-D) reveal the spectroscopy results at high frequency range, which stands for series resistance and SEI resistance, electrode based on POP/bi-ZIF-A1 stay stable at low resistance level (<5 ohm) over 120 cycles. It indicates that both POP/bi-ZIFs demonstrate good structural and electrochemical stability. The electrode based on

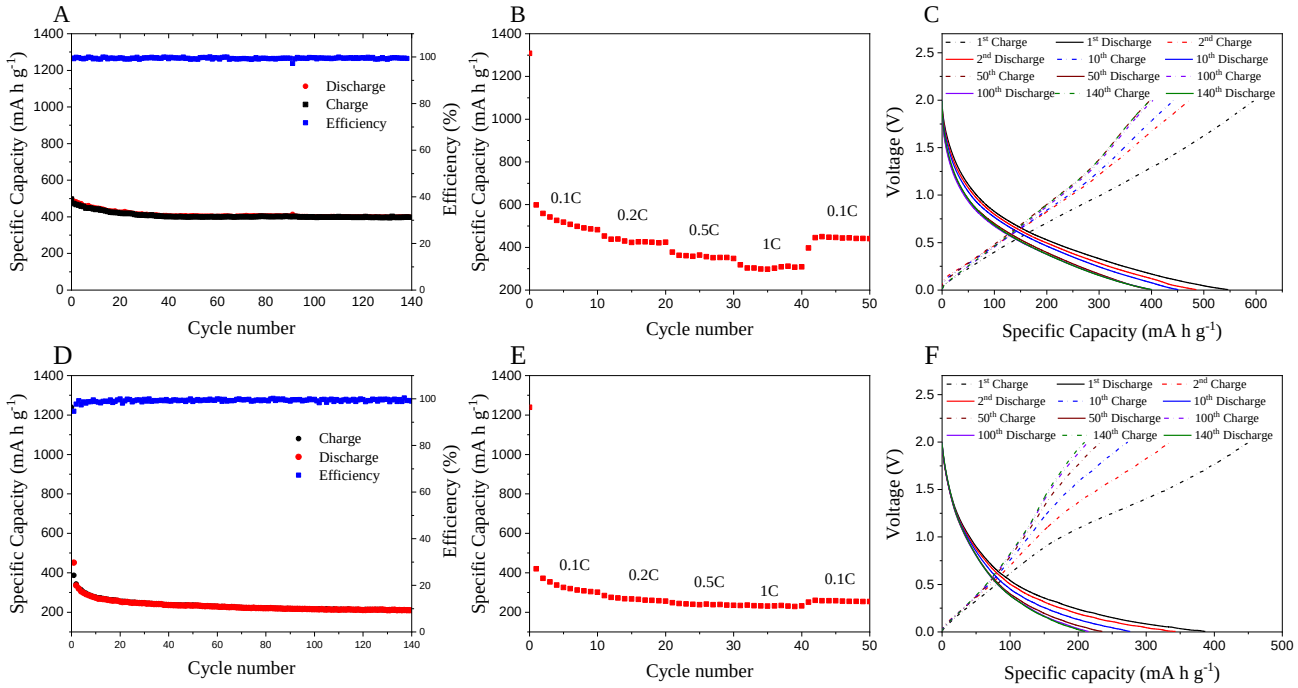

Figure 9 (A) Long term cyclability; B) rate capability; C) successive charge and discharge cycles POP/bi-ZIF-A1 core@shell structure and D) long term cyclability; E) rate capability; F) successive charge and discharge cycles POP/bi-ZIF-D1 core@shell structure

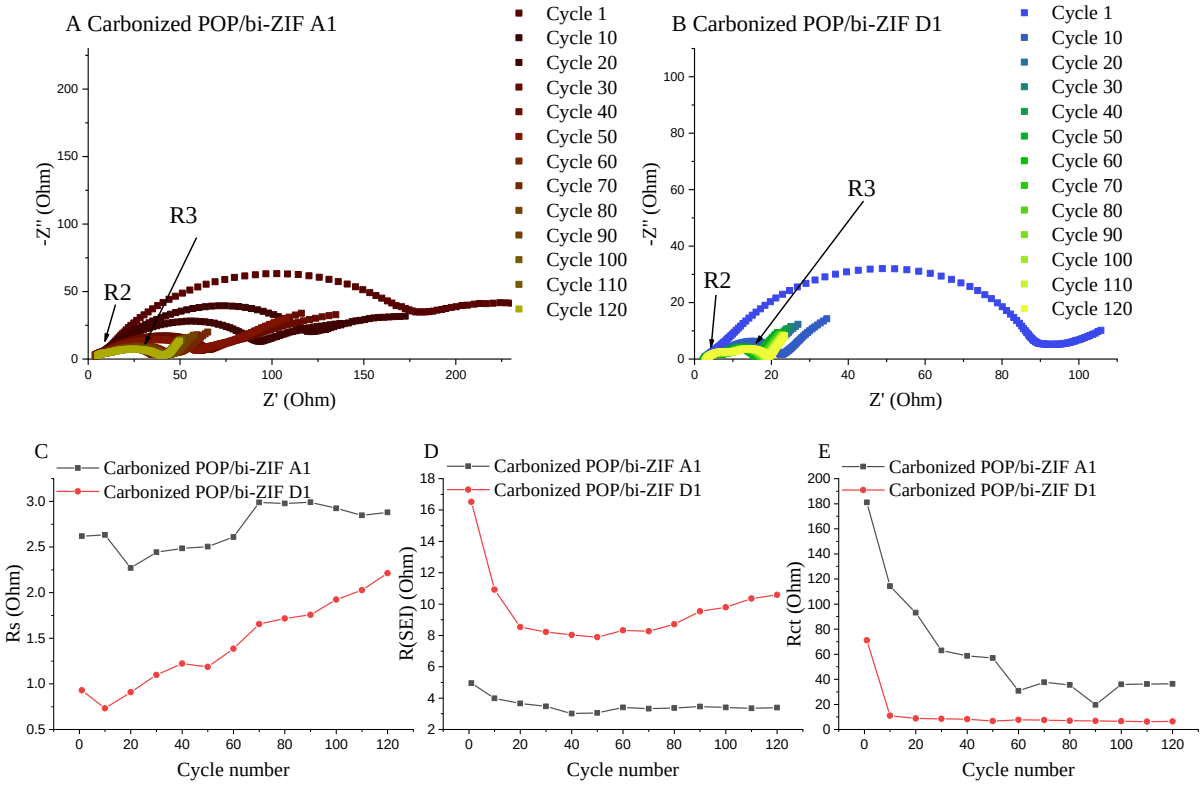

Figure 10 Nyquist impedance spectra of A) carbonized POP/bi-ZIF-A1 and B) carbonized POP/bi-ZIF D1 over cycling; the impedance fitting result of C) series resistance, D) SEI resistance and E) charge transfer resistance

POP/bi-ZIF-D1 showed an increasing series resistance, indicating a declining ionic conductivity, which agrees with the rate stability results. Large SEI resistance was observed at the start from both samples shown in Figure 10A, 10B and 10D, and the SEI resistance dropped significantly after 10-20 cycles for both samples. This is because the large surface area of the carbonized samples takes time to form the SEI layer. After 20 cycles, POP/bi-ZIF-A1 based electrode showed a low and stable SEI resistance (<5 ohm) over 120 cycles, indicating the SEI stabilized quickly in sample A1 which can avoid further capacity loss. POP/bi-ZIF-D1 electrode showed a massive resistance loss after the first 20 cycles, but then it started to increase with cycle number (Figure 10D). This indicates that the SEI in sample POP/bi-ZIF-D1 was very unstable and the SEI has defects and reforms to stabilize during cycling, which loses more irreversible capacity when compared to POP/bi-ZIF-A1. Figure 10E shows the fitting results of charge transfer impedance, which is represented in the impedance spectroscopy at medium frequency range for POP/bi-ZIF A1 and D1. They were both dramatically decreasing over cycling, while the phase angles of Warburg impedance were increasing concurrently. This implies that there is phase transfer over cycling on the POP/bi-ZIFs and it improves the charge transfer resistance on the surface, which is favourable for high rate performance. The electrode based on carbonised POP/bi-ZIF-D1 reached a stable lithiated phase much quicker than A1. Combining with the capacity results, it indicated that D1 was less active than A1. It agrees with the theory stated above that Co itself didn't get involved directly in the insertion and extraction of the Li^+.

POP/bi-ZIF-A1 has the lowest Co:Zn molar ratio, while POP/bi-ZIF-D1 has the highest Co:Zn molar ratio. The carbonised POP/bi-ZIF-A1 showed higher capacity and cycling stability than that of D1. It is reasoned that Co is hard to alloy with Li as compared to Zn, so the conversion mechanism of ZIF-8 working with Li is not applied here.[40] As we discussed above, the higher Co content led to larger size and aggregation of the core@shell particles, which will increase the equivalent series resistance and also restrain the pseudocapacitance of Co. As a result, this will reduce the performance of the anode material and the battery.[40]

4. Conclusion

This paper has provided a facile approach to obtain highly porous core@shell carbon materials with rich heteroatoms and dual-metallic contents at room temperature, with optimised synthesis conditions. The resulting samples represented easily tuneable morphology, structure and metal contents, and showed higher capacity and rate performance than traditional graphite electrode.

Hybrid ZIF-8/ZIF-67 bi-ZIF nanocrystals were synthesised at different conditions. The average crystal size of bi-ZIFs increased from 164 ± 60 nm to 337 ± 130 nm with increasing of Co:Zn ratios from 1:9 to 9:1. The bi-ZIF nanocrystals were further synthesised in the presence of POP nanopheres at optimised conditions and formed POP/bi-ZIF core@shell structures. The bi-ZIF crystals retained their pristine ZIF crystal structure in the POP/bi-ZIF core@shell structures as

characterised by SEM, FTIR and XRD. After carbonisation at 850°C, the resultant hierarchal mesoporous nanocarbon structures showed a BET surface area larger than 1000 m^2 g^{-1}. The carbonized POP/bi-ZIF core@shell nanocarbon with Co:Zn molar ratio of 1:9 exhibited steady cycling stability with a consistent capacity over 400 mA h g^{-1} after 140 cycles. The carbonised POP/bi-ZIF with Co:Zn molar ratio of 7.5:2.5 showed capacity lower than 372 mA h g^{-1} after 2 cycles and poor cycling stability. The lower Co content in the carbonised POP/bi-ZIF core@shell structure benefits the electrochemical capacity and stability compared to traditional graphite. The POP/bi-ZIF derived core@shell carbon nanostructures showed high rate performance and good synergy effects which are ascribed by the high porosity, *in situ* doped heteroatoms and metal elements.

Conflicts of interest

The authors declare no competing interests

Acknowledgements

Y.Z. thanks the research facility support from the International Institute for Nanocomposites Manufacturing (IINM), WMG, University of Warwick, UK.

References

1. X. Jiang, X. Zhu, X. Ai, H. Yang and Y. Cao, *ACS Applied Materials and Interfaces*, 2017, **9**, 25970-25975.
2. C. Li, X. Lou, M. Shen, X. Hu, Z. Guo, Y. Wang, B. Hu and Q. Chen, *ACS Applied Materials and Interfaces*, 2016, **8**, 15352-15360.
3. L. Wang and X. Hu, *Chemistry – An Asian Journal*, 2018, **13**, 1518-1529.
4. S. Jian, W. Yang, W. Lin, J. Hu and L. Zhang, *J. Porous Mater.*, 2017, **24**, 1079-1088.
5. S. Zhu, J. Sun, T. Wu, X. Su, H. Su, S. Qu, Y. Xie, M. Chen and G. Diao, *RSC Advances*, 2016, **6**, 83185-83195.
6. M. M. Thackeray, C. Wolverton and E. D. Isaacs, *Energy and Environmental Science*, 2012, **5**, 7854-7863.
7. S. Cao, T. D. Bennett, D. A. Keen, A. L. Goodwin and A. K. Cheetham, *Chem. Commun.*, 2012, **48**, 7805-7807.
8. K. T. Butler, S. D. Worrall, C. D. Molloy, C. H. Hendon, M. P. Attfield, R. A. W. Dryfe and A. Walsh, *Journal of Materials Chemistry C*, 2017, **5**, 7726-7731.
9. H. Yang, X. W. He, F. Wang, Y. Kang and J. Zhang, *J. Mater. Chem.*, 2012, **22**, 21849-21851.
10. L. T. Nguyen, K. K. Le, H. X. Truong and N. T. Phan, *Catalysis Science & Technology*, 2012, **2**, 521-528.
11. C. Avci, J. Ariñez-Soriano, A. Carné-Sánchez, V. Guillerm, C. Carbonell, I. Imaz and D. Maspoch, *Angewandte Chemie - International Edition*, 2015, **54**, 14417-14421.
12. J. Kim, C. Young, J. Lee, Y. U. Heo, M. S. Park, M. S. A. Hossain, Y. Yamauchi and J. H. Kim, *Journal of Materials Chemistry A*, 2017, **5**, 15065-15072.
13. S. S. A. Shah, L. Peng, T. Najam, C. Cheng, G. Wu, Y. Nie, W. Ding, X. Qi, S. Chen and Z. Wei, *Electrochim. Acta*, 2017, **251**, 498-504.
14. C. Jiao, M. Li, R. Ma, C. Wang, Q. Wu and Z. Wang, *Talanta*, 2016, **152**, 321-328.
15. K. Zhou, B. Mousavi, Z. Luo, S. Phatanasri, S. Chaemchuen and F. Verpoort, *Journal of Materials Chemistry A*, 2017, **5**, 952-957.
16. M. L. Foo, R. Matsuda and S. Kitagawa, *Chem. Mater.*, 2014, **26**, 310-322.
17. M. Jiang, X. Cao, D. Zhu, Y. Duan and J. Zhang, *Electrochim. Acta*, 2016, **196**, 699-707.
18. M. H. Sun, S. Z. Huang, L. H. Chen, Y. Li, X. Y. Yang, Z. Y. Yuan and B. L. Su, *Chem. Soc. Rev.*, 2016, **45**, 3479-3563.
19. Z. Li, L. Zhang, X. Ge, C. Li, S. Dong, C. Wang and L. Yin, *Nano Energy*, 2017, **32**, 494-502.
20. J. Tang, R. R. Salunkhe, H. Zhang, V. Malgras, T. Ahamad, S. M. Alshehri, N. Kobayashi, S. Tominaka, Y. Ide and J. H. Kim, *Scientific reports*, 2016, **6**, 30295.
21. D. Saliba, M. Ammar, M. Rammal, M. Al-Ghoul and M. Hmadeh, *J. Am. Chem. Soc.*, 2018, **140**, 1812-1823.
22. Y. Lü, Q. Zhou, L. Chen, W. Zhan, Z. Xie, Q. Kuang and L. Zheng, *CrystEngComm*, 2016, **18**, 4121-4126.
23. J. K. Zareba, M. Nyk and M. Samoć, *Cryst. Growth Des.*, 2016, **16**, 6419-6425.
24. M. Li, J. Wang, C. Jiao, C. Wang, Q. Wu and Z. Wang, *J. Sep. Sci.*, 2016, **39**, 1884-1891.
25. W. Guo, W. Xia, K. Cai, Y. Wu, B. Qiu, Z. Liang, C. Qu and R. Zou, *Small*, 2017, **13**, 1-8.
26. X. Song, S. Chen, L. Guo, Y. Sun, X. Li, X. Cao, Z. Wang, J. Sun, C. Lin and Y. Wang, *Advanced Energy Materials*, 2018, **1801101**, 1801101.
27. Q. Niu, J. Guo, B. Chen, J. Nie, X. Guo and G. Ma, *Carbon*, 2017, **114**, 250-260.
28. Y. Pan, K. Sun, S. Liu, X. Cao, K. Wu, W.-C. Cheong, Z. Chen, Y. Wang, Y. Li and Y. Liu, *J. Am. Chem. Soc.*, 2018.
29. M. Shao, Q. Chang, J.-P. Dodelet and R. Chenitz, *Chem. Rev.*, 2016, **116**, 3594-3657.
30. C. Wan and X. Huang, *Materials Today Communications*, 2017, **11**, 38-60.
31. Y. Zhou, Q. Huang, C. T. J. Low, R. I. Walton, T. McNally and C. Wan, *New J. Chem.*, 2019, **43**, 5632-5641.
32. J. Wei, Y. Hu, Y. Liang, B. Kong, J. Zhang, J. Song, Q. Bao, G. P. Simon, S. P. Jiang and H. Wang, *Adv. Funct. Mater.*, 2015, **25**, 5768-5777.
33. K. Chen, X. Huang, C. Wan and H. Liu, *Chem. Commun.*, 2015, **51**, 7891-7894.
34. J. Cravillon, S. Münzer, S.-J. Lohmeier, A. Feldhoff, K. Huber and M. Wiebcke, *Chem. Mater.*, 2009, **21**, 1410-1412.
35. J. Cravillon, R. Nayuk, S. Springer, A. Feldhoff, K. Huber and M. Wiebcke, *Chem. Mater.*, 2011, **23**, 2130-2141.
36. X. He, C. Yang, D. Wang, S. E. Gilliland, D. R. Chen and W. N. Wang, *CrystEngComm*, 2017, **19**, 2445-2450.
37. Y. Pan, Y. Liu, G. Zeng, L. Zhao and Z. Lai, *Chem. Commun.*, 2011, **47**, 2071-2073.
38. K. Y. Andrew Lin and W. D. Lee, *Chem. Eng. J.*, 2016, **284**, 1017-1027.
39. L. Zhang, Z. Su, F. Jiang, L. Yang, J. Qian, Y. Zhou, W. Li and M. Hong, *Nanoscale*, 2014, **6**, 6590-6602.
40. Z. Li, X. Huang, C. Sun, X. Chen, J. Hu, A. Stein and B. Tang, *Journal of Materials Science*, 2017, **52**, 3979-3991.

41. Q. Liu, L. Yu, Y. Wang, Y. Ji, J. Horvat, M.-L. Cheng, X. Jia and G. Wang, *Inorg. Chem.*, 2013, **52**, 2817-2822.
42. L. Wang, Z. Wang, L. Xie, L. Zhu and X. Cao, *ACS Applied Materials & Interfaces*, 2019, **11**, 16619-16628.
43. Y. Zhou, R. Tian, H. Duan, K. Wang, Y. Guo, H. Li and H. Liu, *J. Power Sources*, 2018, **399**, 223-230.
44. S. Chu and A. Majumdar, *Nature*, 2012, **488**, 294.
45. K. N. Wood, R. O'Hayre and S. Pylypenko, *Energy & Environmental Science*, 2014, **7**, 1212-1249.
46. P. Simon, Y. Gogotsi and B. Dunn, *Science*, 2014, **343**, 1210-1211.
47. S. S. Zhang, K. Xu and T. R. Jow, *J. Power Sources*, 2004, **129**, 275-279.